DOI 10.24425/aee.2024.150892

Design of a six-phase surface mounted permanent magnet synchronous motor with application to electric trucks

VUONG DANG QUOC [1,2]✉, TRINH TRUONG CONG [1]

[1] *Laboratory of High Performance electric machines (HiPems) Vietnam*

[2] *School of Electrical and Electronic Engineering, Ha Noi University of Science and Technology Vietnam*

e-mail: ✉ *vuong.dangquoc@hust.edu.vn*

(Received: 24.11.2023, revised: 22.08.2024)

Abstract: As we have known, permanent magnet synchronous motors (PMSMs) have garnered widespread interest across various industrial applications thanks to their advantages such as high efficiency, reliable performance, simple structure, and adaptability to various shapes and sizes. Due to characteristics of the high torque and low speed, the PMSMs make particularly well-suited for traction applications such as trucks, ship propulsion, mining, and more. In this context, a combination of the analytical method and finite element method (FEM) is proposed for designing and simulating a six-phase surface-mounted PMSM. Firstly, a model of the six-phase PMSM is analytically design to make required/main dimensions. The FEM is then applied to analyse and verify electromagnetic parameters such as of the current waveform, back electromagnetic force (EMF), magnetic flux density in the air gap, flux linkage, torque, cogging torque, torque ripple and harmonic components. Via the obtained results, the research will give a contribution of valuable insights for optimizing the design, performance and reliability for this motor in diverse industrial applications.

Key words: analytical model, back electromotive force (EMF), cogging torque, finite element method, six-phase surface-mounted PMSM, torque ripple

1. Introduction

Permanent magnet synchronous motors (PMSMs) are becoming increasingly relevant to research in the sectors of industrial and electric traction due to their high torque, power density, efficiency, wide speed range, and dependability [1–7]. As a result, they are frequently utilized in applications such as electrical drive systems, collaborative robotics, electric trucks, and automobiles. Three phase PMSMs have been the subject of numerous studies in the past, however there are still

certain restrictions and disadvantages when using these motors in electric trucks [1]. Initially, while being the least expensive alternative when compared to other multi-phase motors, three-phase motors have problems with high induced voltage and low fault tolerance [1]. Within various winding configurations, the choice of the distributed winding is common due to its ability to provide high saliency, thereby enhancing maximum speed and power through flux weakening. Nevertheless, the distributed winding comes with drawbacks such as an extended end winding, a low slot fill factor, and notable torque ripple. Finally, despite the favorable motor performance offered by rare-earth NdFeB permanent magnets (PMs), the associated high cost, an unstable rare-earth supply chain, and low resistance pose significant challenges [1]. Hence, to improve the fault tolerance capabilities, high reliability and output power density of these machines in practical applications, six-phase PMSMs have been recently studied to be used for electric vehicle application. In [2], the authors studied the modeling and analysis of a six-phase surface-mounted PMSM (SPMSM) with an internal rotor. The paper based on equivalent magnetic circuits to encompasses a comprehensive exploration of the behavior and characteristics of machines. A mathematical model developed for the six-phase interior permanent magnet synchronous motor (IPMSM) using the d, q-axis theory was presented in [3]. In this model, the exact relationships among various per-unitized machine parameters, with the goal of optimizing performance in both inverter control (IC) and traction scenarios was applied to control the torque with different speed ranges. Or in [4], a six-phase PMSM with fractional-slot concentrated windings was presented. The FEM was introduced to design a stator housing with dual three-phase windings spaced 75 degrees apart, accompanied by a rotor fitted with ferrite permanent magnets (PMs) arranged in a spoke configuration. An inventive six-phase double-delta PMSM with a toroidal winding (TW) configuration was introduced for the investigation of the magnetic field distribution, back electromotive force (EMF), output torque and losses [5]. This study entails the uniform winding of each coil of the TWs onto the stator yoke in the same direction. The obtained results indicate that when compared to the traditional six-phase PMSM, the proposed six-phase direct-drive PMSM with TWs will exhibits highly advantageous characteristics for direct-drive systems, manifesting in improved low-speed performance and increased the output torque. Another design methodology specifically crafted for multi-phase PMSMs powered by pulse-width modulation voltage source inverters was mentioned in [6]. Initially, the paper focused on highlighting the potential for improving the torque density via the utilization of harmonics. Then, the unique challenges arising from the design process when dealing with multi-phase machines powered by the pulse-width modulation based on power supplies was performed. In [7, 8], an innovative winding arrangement for six-phase PM machines with combination of 18 slots and 8 poles was designed to mitigate undesirable space harmonics of magnetomotive force in the stator. As a result, it contributed to improvements in power/torque density and efficiency, while simultaneously reducing eddy current losses in PMs and copper losses in the end windings. To enhance the drivetrain applicability in an electric vehicle (EV), the paper proposed the concept of designing a six-phase PMSM with two distinct three-phase windings. A thorough investigation explored various possible phase shifts between these two sets of windings, considering slot-pole combinations and winding arrangements. The optimal phase shift was then selected based on an analysis of harmonic distributions and their impact on performance of the machine, including eddy current losses of the rotor. In addition, an innovative configuration for a six-phase SPMSM with the 60° phase-belt TW configuration (60°-TW) was proposed by the FEM to analyze magnetic field distribution, back EMF, cogging

torque, output torque and losses [9]. Distinguishing itself from conventional winding methods involving overlapping coils, the 60°-TW employs a unique approach where each coil is wound in the same direction on the stator yoke.

As mentioned above, in order to create the magnetic flux in the air gap, the PM is a crucial component in the PMSM. Due to its high remanence and capacity to operate at high temperatures, Samarium Cobalt (SmCo) was the type of permanent magnet that was commonly used in PMSM prior to the discovery of Neodymium (NdFeB). On the other hand, the discovery of NdFeB represented a major advancement in PMSM design and production. As of right now, the NdFeB is the rare earth magnet with the best magnetic characteristics among all of the magnets in the rare-earth family and is more affordable than SmCo. The NdFeB's primary flaw is that it has a relatively low operating temperature because to its heat sensitivity. SmCo can function steadily at temperatures between 250°C and 550°C, although the NdFeB begins to demagnetize around 80°C. Consequently, research on the demagnetization model of NdFeB is essential for forecasting permanent magnet behavior during PMSM operation. Two models of NdFeB (grade 3512) in machines for electric vehicle applications – linear model and an exponential model – were compared by the authors in [25]. According to the study, the linear model had less residuals than the exponential model around the knee point. Furthermore, for this particular material, the roundness of the knee point cannot always be better described by the exponential model than by the linear model.

Numerous investigations have examined the optimization of PMSM design [26–28]. The author specifically proposed a number of multi-objective optimization methodologies in [29] that could be used to shape the design process of electromagnetic devices in general and PMSM in particular. These methodologies included evolutionary methods (e.g., strength pareto evolutionary algorithm, non-dominated sorting genetic algorithm, etc.), evolution strategy, and the gradient-balance method for 2D problems. Other approaches that could be used include artificial bee colony algorithm [30], particle swarm optimization (PSO) [31], etc. Constraints, objective functions, and variables make up the three fundamental components of any optimization technique. Analytical calculations are necessary and play a significant role in the successful application of optimization methods since they aid in the selection of appropriate variables and the construction of appropriate constraints.

Although, many papers have researched on the six-phase PMSMs as discussed above, there are notable limitations in the quantity of research dedicated to these motors. Specifically, when investigating these types of machines, authors have mainly presented specifications of six-phase PMSMs and also made experiments to define some parameters without giving a detailed design process on these machines.

In this research, a combination of the analytical method and FEM is presented for designing and simulating a six-phase SPMSM. Firstly, a model of the six-phase PMSM is analytically design to make required/main dimensions. Then, the FEM is introduced to analyse and verify electromagnetic parameters such as of the current waveform, back electromagnetic force (EMF), magnetic flux density in the air gap, flux linkage, torque, cogging torque, torque ripple and harmonic components. Via the analytical method, it provides a correct approach for calculating the required dimensions of the proposed motors, which can apply for ranges of power levels before using the FEM to validate the calculations. As mentioned above, the analytical method is also an important step to build the variables, constraints and the objective functions for the optimization process, which could compute the most optimal results for the sizes of the motor. The development of the method is validated on a 115 kW six-phase SPMSM that will be designed in Section 3.

2. Background of a six-phase PMSM

The structure a six-phase SPMSM is shown in Fig. 1. It illustrates the proposed topologies through cross-section and exploded views. These two types of machines employ a six-phase arrangement and an outer-rotor configuration. In Fig. 1(a), the IPM topology presents the PMs inserted within the rotor, whereas Fig. 1(b) shows the type of SPM with PMs positioned on the surface of rotor. It should be noted that that the primary distinction between the IPM and SPM machines lies in the arrangement of PMs.

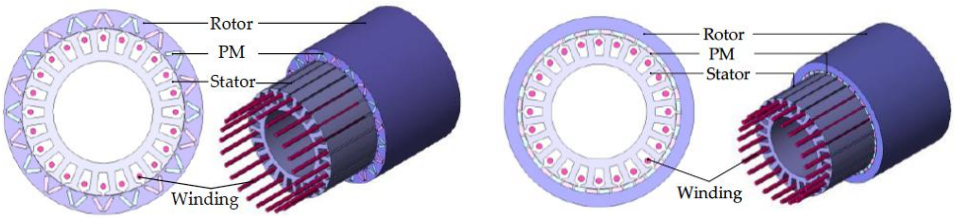

Fig. 1. Modeling of the six-phase-outer rotor PMSM with: IPM type (a); SPM type (b) [13]

It can be seen that the IPM machine incorporates a rotor with V-shaped PM poles. Research indicates that the operation performance of V-shaped PM poles is superior to the traditional radial PM arrangement [23]. Additionally, to prevent short-circuiting of PM fluxes, a magnetic insulation material is deliberately employed. The IPM type features a single-layer fractional slot concentrated winding, effectively reducing the length of end windings and minimizing copper loss [24]. The SPM machine and the IPM type have a common stator structure, but they differ in their PM arrangement. In contrast to the IPM type, which has PMs embedded in its stator, the SPM machine houses PMs on the surface of its rotor.

3. Design of a six-phase SPMSM

In this Section, a six-phase outer rotor SPMSM of a 115 kW with outer rotor configuration is proposed as a reference for this paper. The main parameters of this machine are given in Table 1.

Table 1. Main parameters of the outer rotor SPMSM

Parameter	Value	Unit
Continuous power	115	kW
DC bus voltage	350	V
Number of phases	6	Phase
Number of slots	24	Slot
Number of pole pairs	4	Poles
Continuous torque	1140	Nm

In the design process, magnetic fields in the air gap generated by the PM is very important to determine the parameters such as width, thickness, length and the coverage angle of the PM. The PM material used in this research is the NdFeB, and the demagnetization curves is presented in [19]. The main dimensions of the magnetic core are shown in Fig. 2.

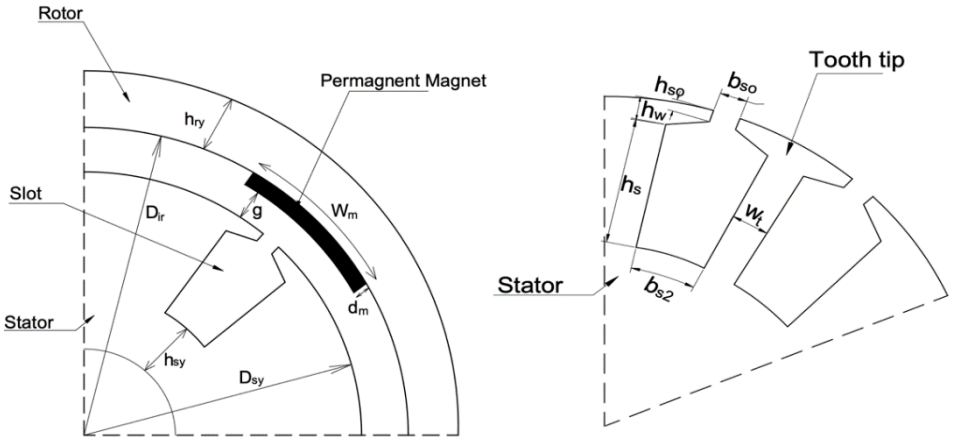

Fig. 2. Main dimensions of the magnetic core (*left*) and slot (*right*) (D_{ir} – dimensions of the magnetic core; g – airgap length; h_{sy} – height of stator yoke; h_{ry} – rotor yoke h_{ry}; L – length of the stator and rotor L; b_{so} – slot open; h_{so} – heith of tooth; w_t – distance between two slots; b_{s1} – above width of slot; b_{s2} – bottom width of slot; h_s – height of slot)

The thickness of the PM is determined following to the below expression:

$$d_m = \frac{\mu_m g_{\text{eff}}}{\frac{B_r \cdot 4\sin(\alpha)}{B_g \pi} - 1}, \tag{1}$$

where: α, μ_m, g_{eff} and B_r are, respectively, the electrical degree, permeability of the PM, effective airgap length and the remanence of the PM. The magnetic flux density in the air gap (B_g) is given by the below equation:

$$B_g = \frac{4}{\pi}\sin(\alpha) B_m, \tag{2}$$

where: B_m is the normal working flux density of the PM. It should be noted that the g_{eff} is used instead of the physical airgap length (g) determined by the Carter's factor (k_c) as given in [12]:

$$g_{\text{eff}} = k_c g. \tag{3}$$

The k_c can be expressed as:

$$k_c = \frac{\tau_s}{\tau_s - \gamma g}, \tag{4}$$

where: the slot pitch (τ_s) is defined as:

$$\tau_s = \frac{\pi(D_{ir} - 2g)}{N_r}, \tag{5}$$

where: D_{ir} and N_r are the inner diameter and number of slots, respectively. The factor (γ) of the PM in (4) already is given in [12], that is:

$$\gamma = \frac{2b_s}{\pi g}\left[\arctan\left(\frac{b_{so}}{2(L+g)}\right) - \frac{L+g}{b_{so}}\ln\sqrt{1+\left(\frac{b_{so}}{2(L+g)}\right)^2}\right], \tag{6}$$

where: b_{so} and L are, respectively, the width of slot opening and length of the PM as already presented in Fig. 2. The width of the PM is determined as:

$$w_m = \frac{\alpha D_{ir}}{p}, \tag{7}$$

where: p is the number of pole pair. The volume of the armature part can be calculated as [12]:

$$\frac{\pi}{4}D_{ir}^2 L = \frac{M_n k_{\text{safe}}}{2\sigma_m}, \tag{8}$$

where: M_n is the rated torque of the motor, σ_m is the value of the shear stress that PM material (NdFeB) ($\sigma_m = 20 - 50$ kPa) [12]. The safe factor (k_{safe}) is the ratio of the rotor length to the inner diameter of the rotor i.e., [12]:

$$k_{\text{shape}} = \frac{L}{D_{ir}}. \tag{9}$$

The height of stator yoke (h_{sy}), rotor yoke (h_{ry}) and width of tooth (w_t) is defined as:

$$h_{sy} = \frac{B_m w_m}{2B_{sy}}, \tag{10a}$$

$$h_{ry} = \frac{B_m w_m}{2B_{ry}}, \tag{10b}$$

$$w_t = \frac{2pB_m w_m}{N_r B_t}, \tag{10c}$$

where: B_{sy}, B_{ry} and w_t are, respectively, the values of magnetic flux density at the stator yoke, rotor yoke and width of tooth. These values were already given in [13].

The number of turns (N_c) per coil is defined as:

$$N_c = \frac{U_{\text{phase}}}{2\pi\sqrt{2} f q k_w B_g \cos\delta D_{ir} L}, \tag{11}$$

where: U_{phase} is the phase voltage, f is the frequency, q is the number of slots per phase per pole, k_w is the winding factor, δ is the torque angle chosen as 20 degrees [2]. The slot area can be calculated as:

$$A_{\text{slot}} = \frac{4N_c A_{Cu}}{k_{fill}}, \tag{12}$$

where: A_{Cu} is the copper area and k_{fill} is filling factor of the slots.

The slot top width (b_{s1}), slot bottom width (b_{s2}) and slot height (h_s) can be obtained as:

$$b_{s1} = \frac{\pi(D_{os} - 2h_{so} - 2h_w)}{Q} - w_t, \tag{13a}$$

$$b_{s2} = \sqrt{b_{s1}^2 - \frac{4\pi}{Q} A_{\text{slot}}}, \tag{13b}$$

$$h_s = \frac{2A_{\text{slot}}}{b_{s1} + b_{s2}}, \tag{13c}$$

where: h_{so} and h_w are respectively the height of the slot opening and the wedge.

Based on the analytical calculation process as presented above, a six-phase outer rotor SPMSM of 115 kW is applied to verify the development of method. The required dimensions of the proposed model are given in Table 2.

Table 2. Required dimensions of a six-phase outer rotor SPMSM of 115 kW

Parameter	Value	Unit
D_{ir}	363.4	mm
L	512	mm
h_{ry}	33.3	mm
g	2	mm
w_m	106.9	mm
d_m	5.2	mm
w_t	20.79	mm
h_s	20.5	mm
b_{s1}	23.8	mm
b_{s2}	18.4	mm
b_{so}	5	mm
h_{so}	2	mm
h_w	2	mm
h_{sy}	33.3	mm
N_c	3	turn
n_c	15	

The cogging torque is a type of intermittent torque that can lead to vibration and noise in PMSMs [15, 16]. When using PMSMs in variable speed drive applications, if the frequency of torque fluctuations aligns with the mechanical resonance frequency of the stator or rotor, it can amplify the vibration and noise originating from the cogging torque. The cogging torque is defined in the following equations [17]:

$$T_{\text{cog}}(\theta) = \frac{2L_a B_\sigma^2 N_s p}{\mu_o \pi N_L} (R_{\text{in}}^2 - R_{\text{out}}^2) T_k, \tag{14}$$

$$T_k = \sum_{k=1}^{\infty} \frac{K_{sk}}{k} \sin\left(kN_L \frac{b_o}{2}\right) \sin\left(kN_L \frac{\alpha_p}{2p}\right) \sin\left(kN_L \left(\theta - \frac{\alpha_s}{2}\right)\right), \tag{15}$$

$$K_{sk} = \frac{2\sin\left(\frac{kN_L\alpha_s}{2}\right)}{kN_L\alpha_s}, \tag{16}$$

where: L_a is the effective axial length of the motor, B_σ^2 is the maximum magnetic flux density in the air-gap, N_s is the number of stator slots, N_L is the lowest common multiple of N_s and 2p, μ_0 is the permeability, R_{in} is the inner radius of air gap, R_{out} is the outer radius of air gap, b_0 is the slot opening, α_p indicates the pole-arc to pole-pitch ratio, α_s is the skewing angle and K_{sk} is the skew factor.

4. Electromagnetic finite element method

The analytical model made it quick to calculate differences in design parameters. But this calculation only permits to define main parameters without presenting electromagnetic parameters of the proposed machine. Consequently, in this section, an FEM is introduced to simulate and verify analytical results. The set of Maxwell's equations and constitutive laws is expressed [34].

$$\nabla \times \boldsymbol{H} = \boldsymbol{J}_s, \tag{17a}$$

$$\nabla \times \boldsymbol{E} = -j\omega B, \tag{17b}$$

$$\nabla \boldsymbol{B} = 0, \tag{17c}$$

$$\boldsymbol{B} = \mu \boldsymbol{H}, \tag{18a}$$

$$\boldsymbol{J} = \sigma \boldsymbol{E}, \tag{18b}$$

where: $\boldsymbol{H}$ is the magnetic field (A/m), $\boldsymbol{J}_s$ is the current density (A/m^2), $\boldsymbol{E}$ is the electric field (V/m), $\boldsymbol{B}$ is magnetic flux density (T) and $\boldsymbol{J}$ is the eddy current density (A/m^2), μ is the relative permeability and σ is electric conductivity (S/m). The field $\boldsymbol{B}$ in (17c) is derived from a vector potential $\boldsymbol{A}$ such that

$$\boldsymbol{B} = \nabla \times \boldsymbol{A}. \tag{19}$$

Combining Eqs. (17b) and (19), the field $\boldsymbol{E}$ is defined via an electric scalar potential φ, that is:

$$\boldsymbol{E} = -\partial_t \boldsymbol{A} - \nabla \cdot \varphi. \tag{20}$$

Based on the equations from (17) to (20), the electromagnetic field equation written in Ω (domain of a PM machine) can be expressed as [9, 18–20]:

$$\nabla \times \left[\frac{1}{\mu} (\nabla \times \boldsymbol{A} - \boldsymbol{B}) \right] + \sigma \partial_t \boldsymbol{A} = \boldsymbol{J}_s - \sigma \nabla \varphi. \tag{21}$$

The below equations, (22), are solved with boundary conditions (BCs), i.e., [34]:

$$\boldsymbol{n} \times \boldsymbol{H}|_{\Gamma_h} = 0, \tag{22a}$$

$$\boldsymbol{n}\, \boldsymbol{B}|_{\Gamma_e} = 0, \tag{22b}$$

where: $\boldsymbol{n}$ is the unit normal exterior to studied domain.

The linkage flux (ϕ) is then defined as:

$$\phi = \frac{L}{S} \left(\iint\limits_{\Omega}^{+} \boldsymbol{A} \mathrm{d}\Omega - \iint\limits_{\Omega}^{-} \boldsymbol{A} \mathrm{d}\Omega \right), \tag{23}$$

where: L is the conductor length and S is the cross-section area of the L. It should be noted that the back EMF is defined via the linkage flux in Eq. (23).

5. Numerical test

Based on the main dimensions of the six-phase outer rotor SPMSM obtained by the analytical model already given in Table 3, the electromagnetic parameters are now verified by the FEM. The B–H curve of electrical steel with code of M350-50A was chosen for magnetic laminations of the proposed machine presented in Fig. 3.

Table 3. Current directions in the six-phase winding

Slots	**Current directions**		**Slots**	**Current directions**		**Slots**	**Current directions**	
1	2+	1+	2	1–	3–	3	3+	2+
	6–	5–		5+	4+		4–	6–
4	2–	1–	5	1+	3+	6	3–	2–
	6+	5+		5–	4–		4+	6+
7	2+	1+	8	1–	3–	9	3+	2+
	6–	5–		5+	4+		4–	6–
10	2–	1–	11	1+	3+	12	3–	2–
	6+	5+		5–	4–		4+	6+
13	2+	1+	14	1–	3–	15	3+	2+
	6–	5–		5+	4+		4–	6–
16	2–	1–	17	1+	3+	18	3–	2–
	6+	5+		5–	4–		4+	6+
19	2+	1+	20	1–	3–	21	3+	2+
	6–	5–		5+	4+		4–	6–
22	2–	1–	23	1+	3+	24	3–	2–
	6+	5+		5–	4–		4+	6+

It is evident that for each type of motor, there are perfect locations of flux density (also known as magnetic loading) for the magnetic core portions, which may be in a linear or non-linear zone depending on the power level. When used in the design process, these considerations can have an impact on the motor's noise level, vibration, torque quality, and other characteristics. To determine these optimum points, optimization procedures and iteration techniques (such as fixed-point iteration, Newton iteration, etc.) must be used. Nevertheless, this problem was overlooked by the authors of this study, who simply selected a flux density value within each component's permitted range to use in the design and computation of the magnetic core's dimensions. The information about magnetic loading of salient-pole PMSMs can be found in [32, 33].

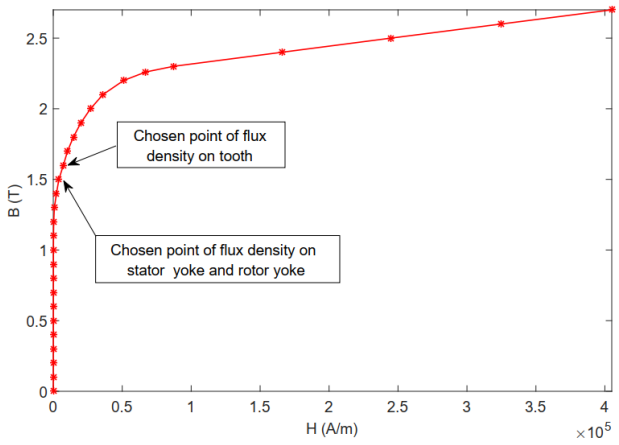

Fig. 3. The B–H curve of electrical steel with code of M350-50A

The 2D geometry of this motor is pointed out in Fig. 4. The model of winding configurations of a six-phase outer rotor SPMSM is shown in Fig. 5, where current directions in the six-phase winding are given Table 3.

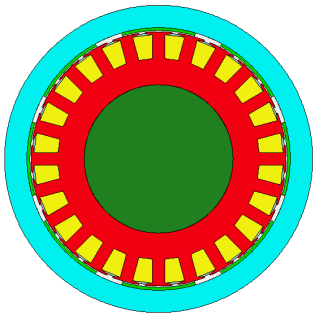

Fig. 4. Geometry of the proposed motor in 2D

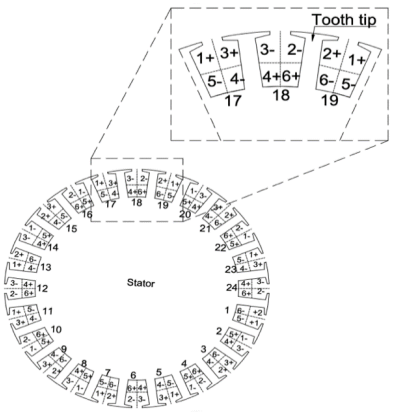

Fig. 5. Model of winding configurations of a six-phase outer rotor SPMSM

The waveform of current distribution is pointed in Fig. 6. In this design, a skewing technique for PMs in the rotor is proposed to get the sinusoidal waveform of the back EMF. The use of step skewing PMs, a widely adopted approach for mitigating cogging torque and minimizing torque ripple is employed. This method not only adjusts the distribution of electromagnetic forces on the stator but also significantly impacts the motor's emitted noise [14]. To perform the skewing technique, each PM needs to be divided into 5 slices (segments) as shown in Table 4. The model of skewing PMs is presented in Fig. 7. However, these angles can be chosen via an optimization process to obtain the best result with the minimum torque ripple.

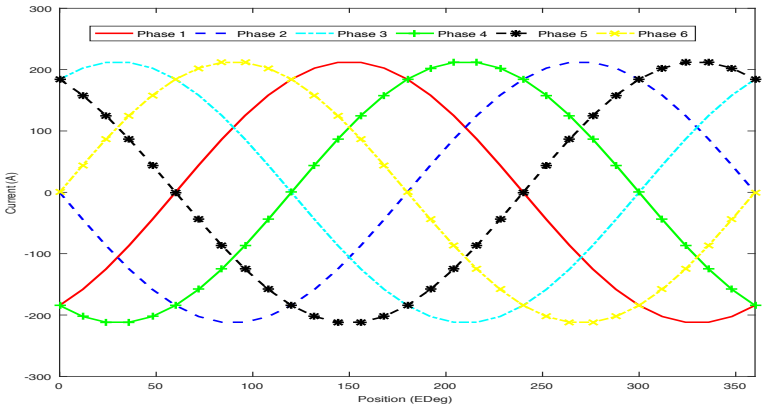

Fig. 6. Current waveform of the six-phase outer rotor PMSM

Table 4. Skew angles of the PM

Slice	**Length of slice**	**Skewed angle (degree)**
Slice 1	1	–6
Slice 2	1	–3
Slice 3	1	0
Slice 4	1	3
Slice 5	1	6

For the no-load case, the back EMF distribution is pointed out in Fig. 8. It can be seen that the waveform is almost sinusoidal, which is the expected output result. The harmonic order of the back EMF with the harmonic distortion of 2.785% is shown in Fig. 9. The simulation results such as the output power, shaft torque, power factor, back EMF and efficiency are given in Table 5. It can be seen that the output power is 115210 W and 1158 Nm for the shaft torque. These values are perfectly satisfied the design requirements. The phase back EMF is 137.6 V, which is a little bit smaller than the phase terminal voltage as a requirement. The maximum torque is 1193.7 Nm, this value is the maximum possible PM and reluctance torque. Normally, the magnetic core of the

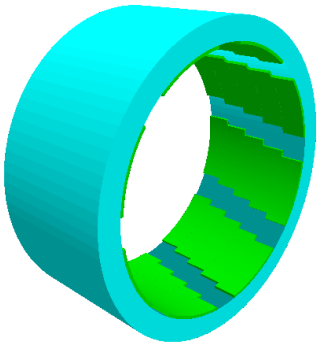

Fig. 7. Skewing PM with different angles given in Table 5

three-phase and six-phase motor are almost the same, including the dimensions of magnet, stator and rotor except for differences in the teeth and slots number. In a six-phase machine, the number of slots and teeth is double that in a three-phase machine.

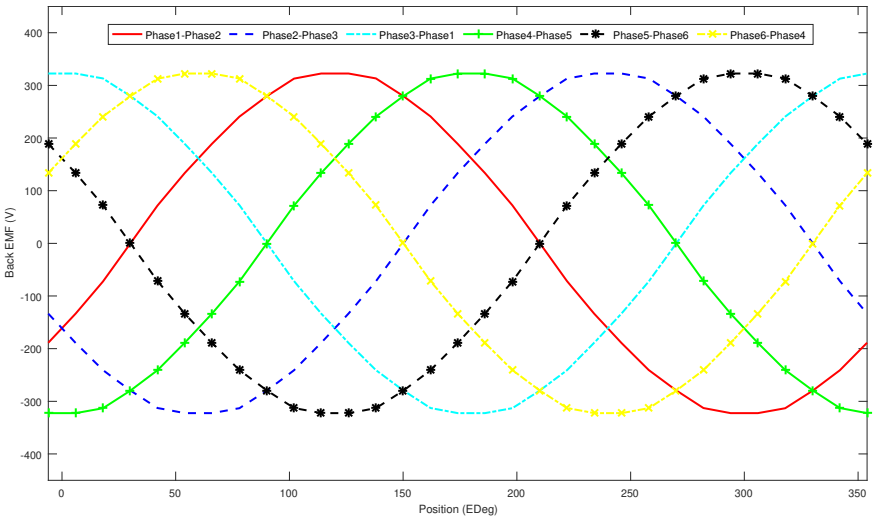

Fig. 8. No-load back EMF waveform

However, there exists a slight discrepancy in the iron loss when comparing three-phase and six-phase motors. This discrepancy pales in significance when juxtaposed with the copper loss observed in both machine types. An equal number of turns per coil can be achieved since the characteristics D_{ir} and L remain consistent in both motor variants. But, the six-phase motor boasts twice the number of phases, slots, and turns within each slot in comparison to the three-phase motor. These collective factors culminate in a situation where: the copper loss in the six-phase motor surpasses that of the three-phase motor, consequently diminishing overall efficiency. The magnet loss is also calculated via the numerical method. It's also a part of the total loss but it was not mentioned. We interpreted the iron loss and the copper loss in the study because they are general and they are true for most circumstances. However, the magnet loss is different. The

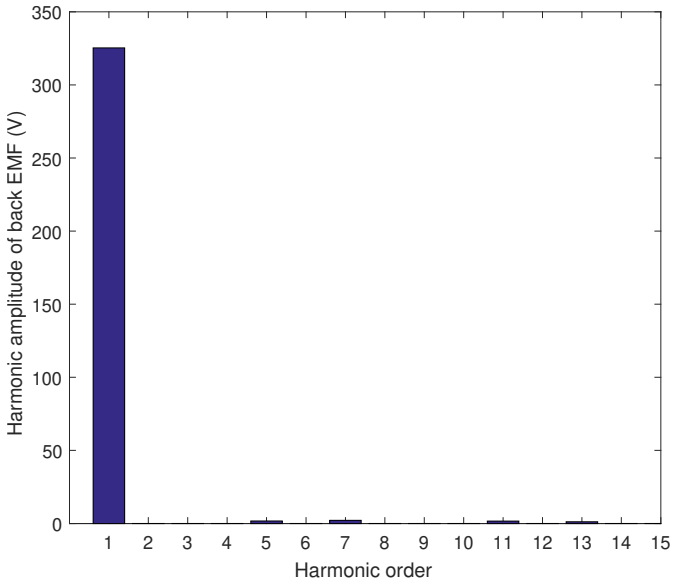

Fig. 9. Harmonic components of the back EMF

Table 5. Simulation results

Parameter	**Value**
Output power (W)	115 210
Maximum torque (Nm)	1193.7
Shaft torque (Nm)	1158
Efficiency (%)	94.42
Power factor	0.976
Phase back EMF (V)	137.6

changes of this loss are quite complex and they depend on many factors. One of the most influential factors is the combination of the number of pole-slots. And because the behavior of magnet loss is not the same in different situations so it cannot be explained in a general way like the iron loss and copper loss. The 2D element mesh of the proposed motor is shown in Fig. 10.

It can be seen that in the air gap region, the element mesh is very thin compared to the remaining parts. This is because air gap is a crucial part of the motor. It is the intermediate part where the interaction between stator and rotor takes place, the magnetic flux must flow through the air gap when it moves from stator and rotor or vice versa. Moreover, the shape and length of air gap also play a significant role in output parameters of motor, such as noise, vibration, back EMF and torque waveform, etc. Therefore, the use of thin mesh in the air gap makes the simulation process more efficient and the results will be more accurate. The magnetic flux density distribution with the symmetry of the motor is shown in Fig. 11.

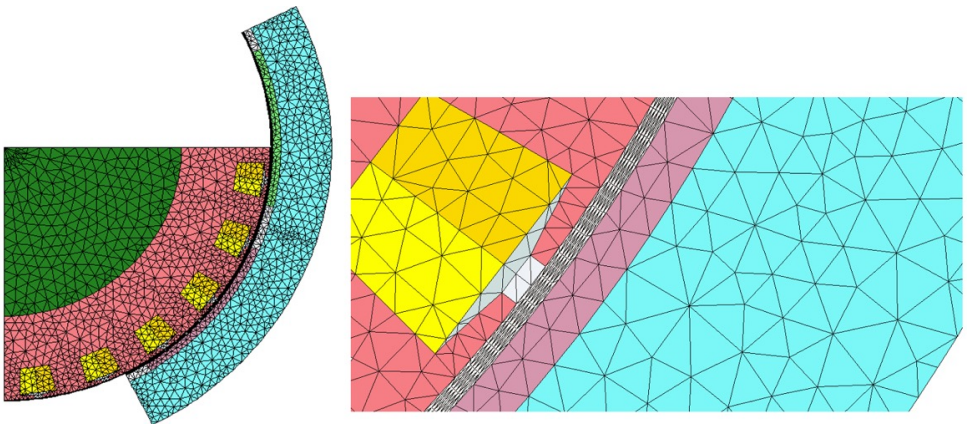

Fig. 10. 2D element mesh of the proposed motor (*left*) and a zoom of air gap and slot

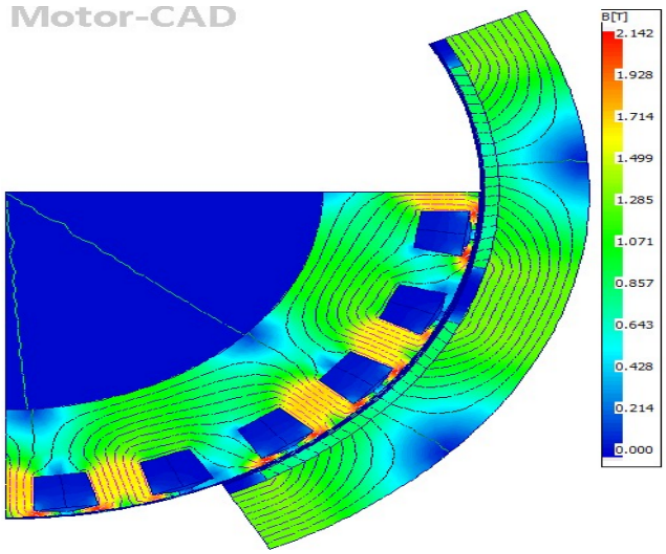

Fig. 11. Magnetic flux density distribution with the symmetry

The maximum value of the flux density is 2.142 T, which is completely acceptable. The higher value of flux density concentrates on the teeth and the corner of tooth tips due to the small area while the other parts of the core have the smaller value of flux density. The magnetic flux density waveform in the air gap under no load operations is indicated in Fig. 12, including the total, the radial, and the tangential air gap flux density. The motor type in this study is the radial flux motor, therefore we concentrate more on the radial component as it's the main component of flux density in the air gap.

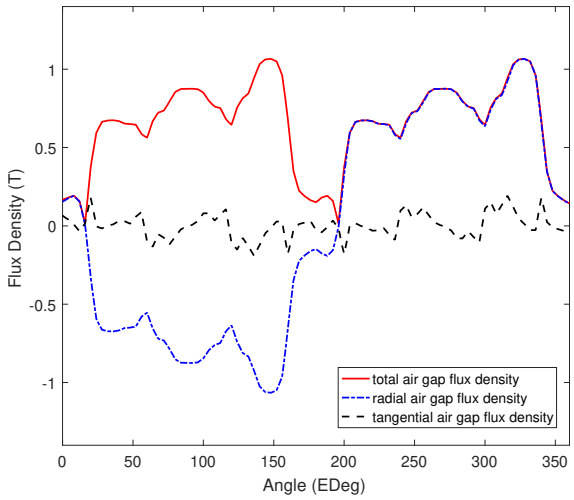

Fig. 12. Waveform of flux density distribution at the air gap

The maximum value is 1.05 T with the position of rotor of 150 and 330 degrees. The amplitudes of high harmonic components are presented in Fig. 13.

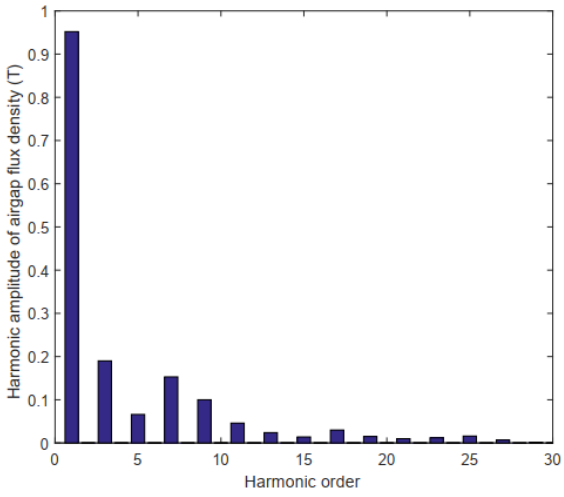

Fig. 13. Harmonic oders of flux density waveform

It is very significant for 3rd, 5th, 7th 9th, 11th, 13th, 15th and 17th orders. The reason for a large deformation of the air gap flux density is the combination of the number of poles and the number of slots. The waveform of this parameter is improved by changing the pole shape through pole trimming, or use other combination of the number of pole-slots. However, this is unnecessary in this paper if you look at the back EMF waveform in Fig. 14. In the same way, the waveform of flux

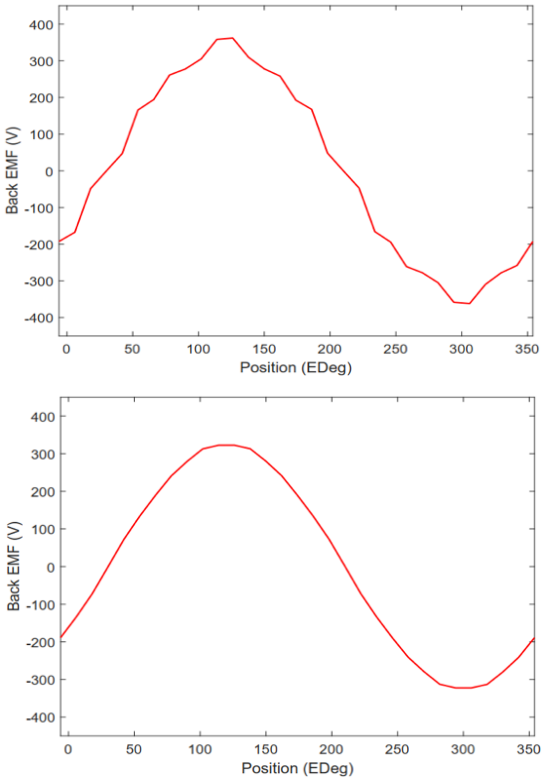

Fig. 14. Phase back EMF waveform with no the skewing technique (*top*) and the skewing technique (*bottom*)

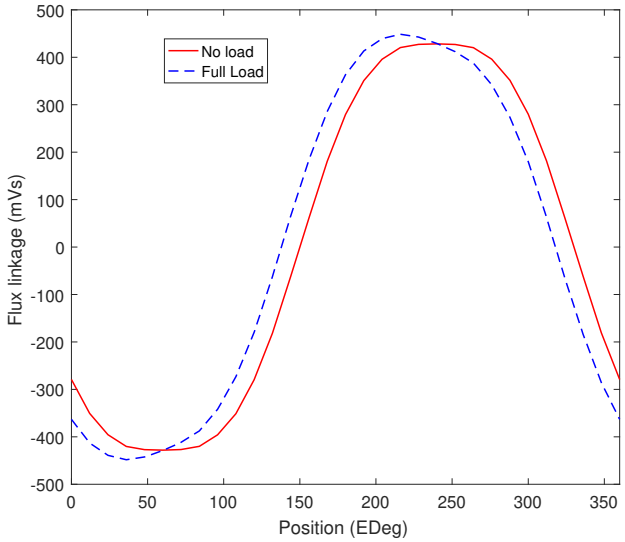

Fig. 15. Distribution of flux linkage waveform

linkage is pointed out in Fig. 15. It can be seen that the amplitude and waveform of flux linkage for two cases are quite similar and sinusoidal. The harmonic amplitude of the flux linkage under no and full load operations is also shown in Fig. 16. The output torque waveform is presented in Fig. 17. It is very smooth with the small value of torque ripple being lower than 2.5% as presented in Fig. 18. The low torque ripple is an important result that the design needs to achieve the expected results. This result means that the motor is working stably and smoothly. The cogging torque waveform is shown in Fig. 19. The peak value reaches nearly 90 Nm.

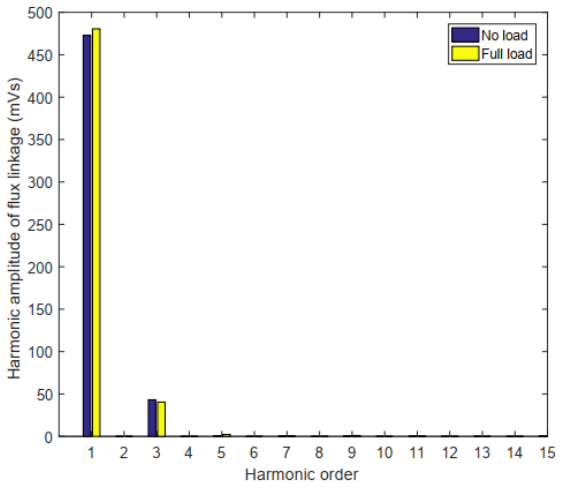

Fig. 16. Harmonic amplitudes of the flux linkage under no and full load operations

It shows that if a motor wants to work well, the EMF needs to be sinusoidal as much as possible. As we see in Fig. 14 (*right*), the deformed waveform of the air gap flux density lead to the back EMF waveform with significant harmonic amplitude. Thanks to the step rotor skewing technique, the back EMF is smoother and more sinusoidal, which is the expected result.

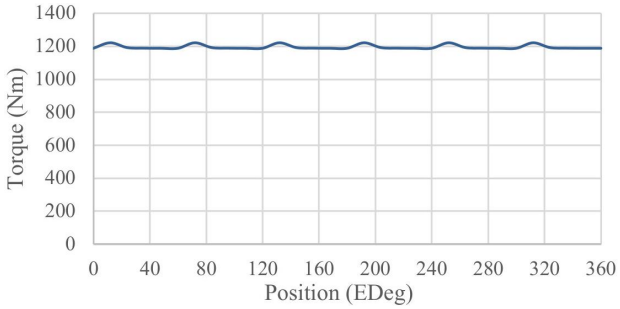

Fig. 17. Output torque waveform

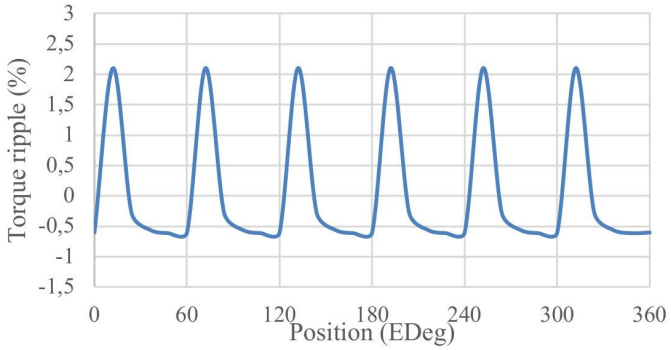

Fig. 18. Torque ripple waveform

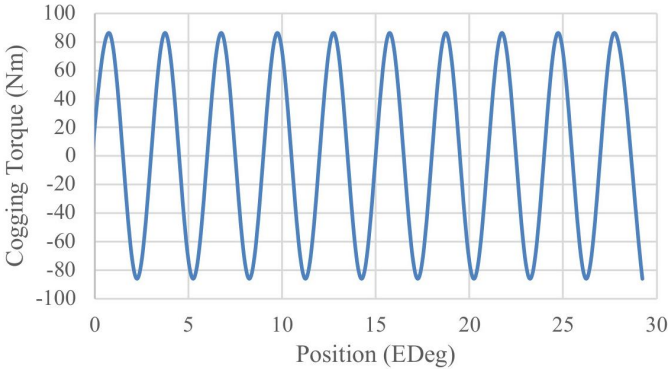

Fig. 19. Cogging torque waveform

6. Conclusions

In this paper, a 115 kW six-phase outer rotor permanent magnet synchronous motor using NdFeB N38 magnet material is designed. The analytical equations for calculating the dimensions of the proposed motor have been successfully. The simulation results have shown that the design achieves the power and the torque requirements with the low torque ripple, which means the analytical method is completely accurate and reliable. The outcomes acquired might be a helpful resource for manufacturers, academics, and designers. This also serves as a basis for numerous other investigations as well, one of them can be applying optimization methods, such as genetic algorithms and particle swarm optimization, etc., to compute the optimal dimensions for the design of the motor. Therefore, the design optimization of this motor to achieve the optimal results in efficiency, cogging torque, torque ripple and cost of the material will be developed in next studies.

Acknowledgements

This research is funded by Hanoi University of Science and Technology (HUST) under project number T2023-PC-043.

References

[1] Del Pizzo A., Di Noia L.P., Di Tommaso A.O., Miceli R., Rizzo R., *Comparison between 3-ph and 6-ph PMSM drives for the electric propulsion of unmanned aerial vehicles*, 2021 IEEE 15th International Conference on Compatibility, Power Electronics and Power Engineering, Italy, pp. 1–5 (2021), DOI: 10.1109/CPE-POWERENG50821.2021.9501082.

[2] Cheng L., Sui Y., Zheng P., Yin Z., Wang C., *Influence of Stator MMF Harmonics on the Utilization of Reluctance Torque in Six-phase PMASynRM with FSCW*, Energies, vol. 11, no. 108, pp. 1–17 (2017), DOI: 10.3390/en11010108.

[3] Iyer L.V., Lai C., Dhulipati H., Mukundan S., Mukherjee K., Kar N., *Investigation of a Six-Phase Interior Permanent Magnet Synchronous Machine for Integrated Charging and Propulsion in EVs*, SAE International Journal of Alternative Powertrains, vol. 7, no. 2, pp. 103–116 (2018), DOI: 10.4271/08-07-02-0006.

[4] Won H., Hong Y.-K., Platt J., Choi M., Bryant B., Choi S., *Six-phase Fractional-slot Concentrated Winding Ferrite Spoke-type Permanent Magnet Synchronous Motor for Electric Truck*, IEEE International Electric Machines & Drives Conference (IEMDC), Hartford, CT, USA, pp. 17–20 (2021), DOI: 10.1109/IEMDC47953.2021.9449491.

[5] Jin F., Si J., Cheng Z., Su P., Dong L., Qi G., *Analysis of a Six-Phase Direct-Drive Permanent Magnet Synchronous Motor with Novel Toroidal Windings*, IEEE Vehicle Power and Propulsion Conference (VPPC), Hanoi, Vietnam, pp. 14–17 (2019), DOI: 10.1109/VPPC46532.2019.8952311.

[6] Islam M.Z., Bonthu S.S.R., Choi S., *Comparison of two different winding topologies for external-rotor five-phase PM-assisted synchronous reluctance motor in vehicle applications*, IEEE International Electric Machines and Drives Conference (IEMDC), Miami, FL, USA, pp. 1–6 (2017), DOI: 10.1109/IEMDC.2017.8002399.

[7] Scuiller F., Semail E., Charpentier J.-F., Letellier P., *Multi-criteria-based design approach of multi-phase permanent magnet low-speed synchronous machines*, Electric Power Applications, IET, vol. 3, no. 2, pp. 102–110 (2009), DOI: 10.1049/iet-epa:20080003.

[8] Patel V.I., Wang J., Wang W., Chen X., *Six-Phase Fractional-Slot-per-Pole-per-Phase Permanent-Magnet Machines with Low Space Harmonics for Electric Vehicle Application*, IEEE Transactions on Industry Applications, vol. 50, no. 4, pp. 2554–2563 (2014), DOI: 10.1109/TIA.2014.2301871.

[9] Yanqi Wei, Si Ji, Cheng Zhiping, Xu Shuai, Dong Lianghui, Liang Jing, *Design and characteristic analysis of a six-phase direct-drive permanent magnet synchronous motor with 60°phase-belt toroidal winding configuration for electric vehicle*, IET Electric Power Applications, vol. 14, no. 13, pp. 2659–2666 (2020), DOI: 10.1049/iet-epa.2020.0083.

[10] Li X., Tan Y., Yan B., Zhao Y., Wang H., *Demagnetization Modeling and Analysis for a Six-Phase Surface-Mounted Field-Modulated Permanent-Magnet Machine Based on Equivalent Magnetic Network*, Energies, vol. 16, no. 16, 6099 (2023), DOI: 10.3390/en16166099.

[11] El-Refaie A., Alexander J.P., Galioto S., Reddy P.B., Huh K., Bock P., Shen X., *Advanced High-Power-Density Interior Permanent Magnet Motor for Traction Applications*, IEEE Transactions on Industry Application, vol. 50, no. 1, pp. 3235–3248 (2013), DOI: 10.1109/ECCE.2013.6646754.

[12] Hung Vu Xuan, *Modeling of exterior outer rotor permanent magnet synchronous machines with concentrated winding*, Doctoral Thesis, Technische Universiteit Delft (2012).

[13] Yao Yuqing, Chunhua Liu, Lee C.H.T., *Quantitative Comparisons of Six-Phase Outer-Rotor Permanent-Magnet Brushless Machines for Electric Vehicles*, Energies, vol. 11, no. 8, 2141 (2018), DOI: 10.3390/en11082141.

[14] Patel V., Wang J., Wang W. *et al*., *Six-phase fractional-slot-per-pole-per phase permanent-magnet machines with low space harmonics for electric vehicle application*, IEEE Trans. Ind. Appl., vol. 50, no. 4, pp. 2554–2563 (2014), DOI: 10.1109/TIA.2014.2301871.

[15] Gao C., Gao M., Si J. *et al*., *A novel direct-drive permanent magnet synchronous motor with toroidal windings*, Energies, vol. 12, no. 3, pp. 1–14 (2019), DOI: 10.3390/en12030432.

[16] Heins G., Ionel D., Thiele M., *Winding factors and magnetic fields in permanent magnet brushless machines with concentrated windings and modular stator cores*, IEEE Energy Conversion Congress and Exposition, Denver, CO, USA, pp. 5048–5055 (2013), DOI: 10.1109/ECCE.2013.6647382.

[17] Zhu L., Jiang S., Zhu Z. *et al*., *Analytical methods for minimizing cogging torque in permanent-magnet machines*, IEEE Trans. Magn., vol. 45, no. 4, pp. 2023–2031 (2009), DOI: 10.1109/TMAG.2008.2011363.

[18] Won Hoyun, Yang-Ki Hong, Minyeong Choi, Jonathan Platt, Briana Bryant, Seungdeog Choi, Shuhui Li, Hwan-Sik Yoon, Timothy A. Haskew, Jongkook Lee *et al*., *Novel Design of Six-Phase Spoke-Type Ferrite Permanent Magnet Motor for Electric Truck Application*, Energies, vol. 15, no. 6 (1997), DOI: 10.3390/en15061997.

[19] Potgieter J., Kamper M., *Double PM-rotor, toothed, toroidal-winding wind generator: a comparison with conventional winding direct-drive PM wind generators over a wide power range*, IEEE Trans. Ind. Appl., vol. 52, no. 4, pp. 2881–2891 (2016), DOI: 10.1109/TIA.2016.2536580.

[20] Zhu Z., Howe D., *Influence of design parameters on cogging torque in permanent magnet machines*, IEEE Trans. Energy Conversion, vol. 15, no. 4, pp. 407–412 (2000), DOI: 10.1109/60.900501.

[21] Madhavan R., Fernandes B., *Axial flux segmented SRM with a higher number of rotor segments for electric vehicles*, IEEE Trans. Energy Convers., vol. 28, no. 1, pp. 203–213 (2013), DOI: 10.1109/TEC.2012.2235068.

[22] Cheng Luming, Yi Sui, Ping Zheng, Zuosheng Yin, Chuanze Wang, *Influence of Stator MMF Harmonics on the Utilization of Reluctance Torque in Six-Phase PMA-SynRM with FSCW*, Energies, vol. 11, no. 1, 108 (2018), DOI: 10.3390/en11010108.

[23] Wang A., Jia Y., Soong W.L., *Comparison of Five Topologies for an Interior Permanent-Magnet Machine for a Hybrid Electric Vehicle*, in IEEE Transactions on Magnetics, vol. 47, no. 10, pp. 3606–3609 (2011), DOI: 10.1109/TMAG.2011.2157097.

[24] Zhang X., Ji J., Zheng J., Zhu X., *Improvement of Reluctance Torque in Fault-Tolerant Permanent-Magnet Machines with Fractional-Slot Concentrated-Windings*, in IEEE Transactions on Applied Superconductivity, vol. 28, no. 3, pp. 1–5 (2018), DOI: 10.1109/TASC.2018.2808293.

[25] Barba P.D., *Multiobjective Shape Design in Electricity and Magnetism*, Springer (2010), DOI: 10.1007/978-90-481-3080-1_1.

[26] Dal Ö., Yildirim M., Kürüm H., *Optimization of Permanent Magnet Synchronous Motor Design by Using PSO*, in 4th International Conference on Power Electronics and their Applications (ICPEA), Elazig, Turkey (2019), DOI: 10.1109/ICPEA1.2019.8911192.

[27] Haifeng Z., Zhi D., Jinghua A.Z., *Optimization Design and Analysis of Permanent magnet synchronous motor based on VC*, in International Conference on Electrical Machines and Systems (ICEMS), Sydney, NSW, Australia (2017), DOI: 10.1109/ICEMS.2017.8055957.

[28] Hamidizadeh S., Alatawneh N., Chromik R.R., Lowther D.A., *Comparisonof Different Demagnetization Models of Permanent Magnet in Machines for Eelectric Vehicle Application*, IEEE Transactions on Magnetic (2015), DOI: 10.1109/TMAG.2015.2513067.

[29] Hwang C.-C., Lyu L.-Y., Liu C.-T., Li P.-L., *Optimal Design of an SPM Motor Using Genetic Algorithms and Taguchi Method*, IEEE Transactions on Magnetics, vol. 44, no. 11, pp. 4325–4328 (2008), DOI: 10.1109/TMAG.2008.2001526.

[30] Liu H., *Design of High-Efficiency Rare-Earth Permanent Magnet Synchronous Motor and Drive System*, Electronic Thesis and Dissertations, STARS (2015).

[31] Juha Pyrhönen T.J.V.H., *Design of Rotating Electrical Machines*, Second Edition, John Wiley & Sons Ltd. (2014), DOI: 10.1002/9781118701591.

[32] Mutluer M., Bilgin O., *An intelligent design optimization of a permanent magnet synchronous motor by artificial bee colony algorithm*, Turkish Journal of Electrical Engineering & Computer Sciences, vol. 24, pp. 1826–1837 (2016), DOI: 10.3906/elk-1311-150.

[33] Song T., Zhang Z., Liu H., Hu W., *Multi-objective optimisation design and performance comparison of permanent magnet synchronous motor for EVs based on FEA*, The Insitution of Engineering and Technology IET, vol. 13, no. 8, pp. 1157–1166 (2019), DOI: 10.1049/iet-epa.2019.0069.

[34] Choi Jang-Young, Park Hyung-Il, Seok Myeong Jang, Lee Sung-Ho, *Design and Analysis of Surface-Mounted PM Motor of Compressor for Electric Vehicles Applications according to Slot/Pole Combinations*, The Transactions of the Korean Institute of Electrical Engineers, vol. 60, pp. 1846–1857 (2011), DOI: 10.5370/KIEE.2011.60.10.1846.